JOURNAL OF PROPULSION AND POWER
Vol. 27, No. 2, March–April 2011

# Numerical Analysis on Flame Kernel in Spark Ignition Methane/Air Mixtures

S. Nakaya*
*Osaka Prefecture University, Sakai-shi, Osaka 598-0021, Japan*
K. Hatori
*National Maritime Research Institute, Mitaka-shi, Tokyo 181-0004, Japan*
M. Tsue† and M. Kono†
*University of Tokyo, Bunkyo-ku, Tokyo 113-8656, Japan*
and
D. Segawa* and T. Kadota*
*Osaka Prefecture University, Sakai-shi Osaka, 598-0021, Japan*

DOI: 10.2514/1.47136

**A flame kernel initiation of methane/air combustible mixtures in the spark ignition process was investigated using a two-dimensional theoretical model including a detailed description of gas-phase chemical kinetics, shock capturing scheme and diffusive molecular transport. Interactions of chemical reactions and diffusive transports of radicals in the process of the flame kernel initiation were investigated. Although the model of plasma might be oversimplified, the qualitative behavior of OH for hydrogen/air mixture agreed well with experimental one. The influences of diffusive molecular transport and ignition energy on the flame kernel initiation were discussed. As a result, in the early stage of the flame kernel development for methane/air mixture, the hot gas expansion was dominated by a flow which was induced by the blast wave and the thermal gas at the electrode gap was self-sustained with an application of minimum ignition energy. The induction time of the flame kernel initiation strongly depended on the ignition energy and effects of preferential diffusion of lighter molecules in the early phase of the flame kernel development are outstanding especially in the case of low ignition energy near the minimum.**

## Nomenclature

$D$ = diffusion coefficient, $\mathrm{m^2/s}$
$E_{\min}$ = minimum ignition energy, mJ
$e$ = total energy, J/kg
$h$ = enthalpy, J/kg
$m_f$ = local mass of hydrogen and carbon atoms, kg
$m_o$ = local mass of oxygen atoms, kg
$p$ = pressure, Pa
$r$ = radial position, m
$z$ = axial position, m
$v_r$ = velocity in radial direction, m/s
$v_r$, $v_z$ = velocity along $r$ and $z$, m/s
$v_z$ = velocity in axial direction, m/s
$\kappa$ = thermal conductivity, W/Km
$\mu$ = viscosity, $\mathrm{Pa \cdot s}$
$\rho$ = density, $\mathrm{kg/m^3}$
$\Phi_l$ = local equivalence ratio

*Subscript*

$i$ = $i$th species

## I. Introduction

IGNITION process is rather important in practical combustion devices where the stable burning, high efficiency, and low emissions are strongly required. In engines and gas turbines, spark ignition initiates the flame kernel and influences its development. The ignition process by the spark discharge is also important in the hazard of the fuel leak. In the modern age, the reduction of pollutant emission of automobiles, such as $\mathrm{NO_X}$ and soot has been strongly required. Internal combustion engines have used new technologies such as the direct fuel injection and lean combustion to reduce emissions and increase combustion efficiency. In addition, various fuels (e.g., hydrogen, methane, propane, natural gas) have been used for internal combustion engines. Therefore, understanding on the ignition process for various fuel mixtures is rather important to ensure successful ignition.

Ignition process is influenced by many parameters such as pressure, temperature, spark energy, the shock wave induced by spark discharge, the flowfield, gas composition, heat loss to the electrode, etc. The minimum ignition energy has been experimentally measured and the results indicate that it is influenced by the spark gap and the equivalence ratio of the mixture [1,2]. Increase in the ignition energy affects the flame speed of the subsequent kernel growth as well as the success or failure of the ignition [3]. The deposition of the energy by the composite sparks has also affects the flame kernel development in quiescent and turbulent conditions [4,5]. Short duration energy deposition produces the strong shock wave and its associated flowfields which have large impact on the flame kernel initiation, and the strong coupling between chemical and physical processes have been observed [4–12].

Flowfields and diffusion process strongly affect the flame kernel initiation. The minimum ignition energy shows a nonlinear behavior for the flow velocity and its behavior changes when the electrode gap changes [12]. Short duration sparks produced the shock wave and its induced flow governs the initial shape of the flowfields [6–8]. Diffusion process of species in the spark ignition process has strong influences on the ignition process and the flame speed. The stretch effect of the small flame kernel in the initial stage of the ignition process is essential features of the ignition mechanism [2], and it is even responsible for failure of the ignition. The competition of the stretch effect and the energy supply has been investigated and there is a critical diameter of the flame kernel which results in the subsequent flame propagation [13,14]. The flame speed also depends on the fuel

---

Received 11 September 2009; revision received 16 March 2010; accepted for publication 22 October 2010.

*Department of Mechanical Engineering.

†Department of Aeronautics and Astronautics.

and the equivalence ratio of the mixture due to the change in the stretch effect [15]. In turbulent premixed flows, flame kernel initiation may not be achieved due to the excessive strain rate [16,17].

A lot of numerical analyses have been conducted to understand the ignition mechanism, and many researchers have focused on the growth rate of the kernel radius and distributions of temperature and radicals [3,8–10]; however, only a few studies focus on the interaction of chemical reactions, flowfields, and diffusion processes. Sensitivity analysis of the thermal conductivity, diffusion parameters, and reaction rate coefficients on flame speed was conducted numerically; however, it only focuses on the flame speed [3]. The minimum ignition energy for four alkanes was calculated using simple chemical reaction scheme and effects of kernel size and equivalence ratio was investigated [18]. The critical radius is greatly influenced by the equivalence ratio [15–17,19]. Stretch effects on the flame kernel growth have widely been discussed. However, the effects of the unsteady molecular diffusion transport on the initial flame kernel development have not been clear, especially in the interactions between chemical reactions and physical transport processes. After an arc discharge, temperature of the hot gas in the electrode gap is rather high and the molecular diffusion of radicals are very active (within 1 $\mu$s), and then the temperature decrease to the vicinity of the flame temperature. Therefore, interactions between radical production and physical transport processes have strong effects on the flame kernel initiation. The induction time of the flame kernel initiation strongly depends on the ignition energy [20]. Therefore, in this study, we numerically investigate the mechanism of the flame kernel initiation in the spark ignition process using a numerical model including detail description of the diffusive transport, the shock wave and chemical reactions. Minimum ignition energy for methane/air mixture is calculated and then the structure of the hot gas before the flame kernel initiation is investigated.

## II. Model Description

Although the role of the plasma in the spark ignition process may be important, theories of the breakdown process spark discharge modes, and plasma characteristics are rather complicated and have not been clear and their models have been oversimplified in most studies. In this study, the energy discharge process of the spark ignition is simplified and heat with a uniform distribution is added in the spark channel. In addition, it is assumed that thermodynamic equilibrium in the hot plasma region is achieved at any time; the process is axisymmetric and the size of the spark channel does not change during the discharging period of the spark energy. The distribution of the electric field inside the flame kernel is neglected; radiation of molecules and the plasma are not taken into account.

A numerical model employs a two-dimensional unsteady symmetric cylindrical coordinate system. Figure 1 shows the distribution of the grids in the numerical domain. The numerical domain is bounded by an adiabatic wall which has a nonslip boundary condition, and the size is 4 mm × 5 mm. To keep the kinematic energy constant in the numerical region, the outer boundary reflects the shock wave (reflecting boundary). We also tested a nonreflecting boundary and the results were not rather different although small fluctuations of parameters due to the shock wave traverse could be observed in the initial stage. The number of grids is 81 × 64. The boundary at $r = 0$ is a symmetric boundary. The black rectangular zone shows an electrode where the surface is defined as isothermal and has a no-slip boundary. The surface temperature of the electrode is fixed to be 298 K and the heat flux $q_{\mathrm{el}}$ to the electrode from closest numerical cells is described by Fourier's law as shown in Eq. (1)

$$q_{\mathrm{el}} = \kappa \frac{T - 298}{\Delta h/2} \tag{1}$$

where $\Delta h$ is the grid width of the closest cell. The diameter of the electrode is 1/16 inches and the gap is the quenching distance of methane/air mixtures measured by Lewis and von Elbe [2]. The gap of the electrodes varies when the equivalence ratio of the mixture changes. When minimum ignition energy is measured, the radius of the spark channel is fixed at 0.172 mm. When large ignition energy is applied to the electrode gap, the radius of the spark channel is broadened. Although the effect of spark duration on minimum ignition energy has been discussed and spark component of the glow discharge has largely effects on the spark kernel initiation [8,10,11], capacity spark component is only taken into account for simplicity in this study. The duration of the capacity spark should be held at 1 $\mu$s in this study. The energy density, which is applied into the spark channel per unit time in the spark discharge duration, is constant with time. The ambient temperature and pressure are 298 K and 0.1013 MPa, respectively, and the equivalence ratio of the mixture is uniform at the start of the spark discharge.

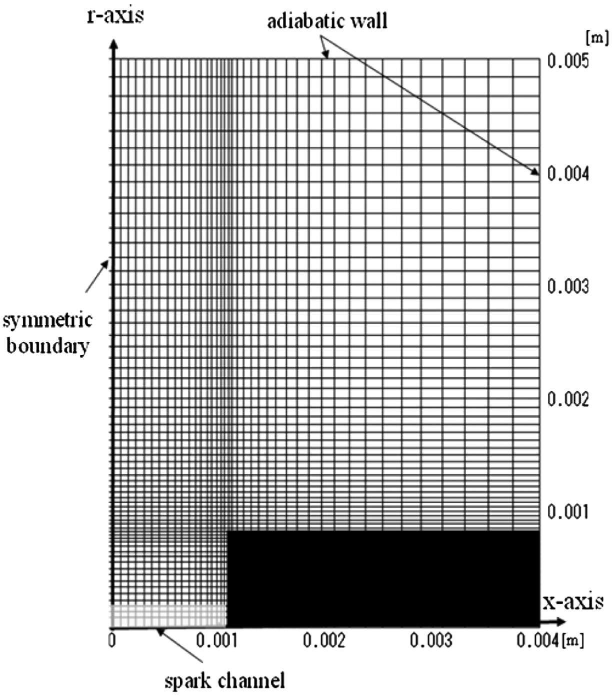

**Fig. 1 Numerical domain and grid distribution.**

The mass, momentum, energy, and chemical species conservation equations are solved numerically. Mass conservation equation is

$$\frac{\partial \rho}{\partial t} + \frac{1}{r}\frac{\partial r \rho v_r}{\partial r} + \frac{\partial \rho v_z}{\partial z} = 0 \tag{2}$$

Compressible Navier–Stokes equations are taken into account and momentum conservation equations are

$$\frac{\partial \rho v_r}{\partial t} + \frac{1}{r}\frac{\partial r \rho v_r^2}{\partial r} + \frac{\partial \rho v_r v_z}{\partial z} = -\frac{\partial p}{\partial r} - \left(\frac{1}{r}\frac{\partial r \tau_{rr}}{\partial r} + \frac{\partial \tau_{zr}}{\partial z} - \frac{\tau_{\theta\theta}}{r}\right) \tag{3}$$

$$\frac{\partial \rho v_z}{\partial t} + \frac{1}{r}\frac{\partial r \rho v_r v_z}{\partial r} + \frac{\partial \rho v_z^2}{\partial z} = -\frac{\partial p}{\partial z} - \left(\frac{1}{r}\frac{\partial r \tau_{rz}}{\partial r} + \frac{\partial \tau_{zz}}{\partial z}\right) \tag{4}$$

where $\tau_{rr}$, $\tau_{\theta\theta}$, $\tau_{rz}$, and $\tau_{zr}$ are stress tensors and expressed as follows:

$$\tau_{rr} = -2\mu \frac{\partial v_r}{\partial r} + \frac{2}{3}\mu \left\{\frac{1}{r}\frac{\partial}{\partial r}(r v_r) + \frac{\partial v_z}{\partial z}\right\} \tag{5}$$

$$\tau_{\theta\theta} = -2\mu \frac{v_r}{r} + \frac{2}{3}\mu \left\{\frac{1}{r}\frac{\partial}{\partial r}(r v_r) + \frac{\partial v_z}{\partial z}\right\} \tag{6}$$

$$\tau_{zz} = -2\mu \frac{\partial v_z}{\partial z} + \frac{2}{3}\mu \left\{\frac{1}{r}\frac{\partial}{\partial r}(r v_r) + \frac{\partial v_z}{\partial z}\right\} \tag{7}$$

$$\tau_{rz} = \tau_{zr} = -\mu \left(\frac{\partial v_r}{\partial z} + \frac{\partial v_z}{\partial r}\right) \tag{8}$$

Energy conservation equation is

$$\frac{\partial \rho e}{\partial t}+\frac{1}{r}\frac{\partial r\rho e v_r}{\partial r}+\frac{\partial \rho e v_z}{\partial z}+\frac{1}{r}\frac{\partial p v_r r}{\partial r}+\frac{\partial p v_z}{\partial z}$$
$$=-\frac{1}{r}\frac{\partial}{\partial r}(rq_r)-\frac{\partial q_z}{\partial z}-\frac{1}{r}\frac{\partial}{\partial r}(\tau_{rr}v_r r+\tau_{rz}v_z r)$$
$$-\frac{\partial}{\partial z}(\tau_{rz}v_r+\tau_{zz}v_v)+\sum_{i=1}^{N}\left\{\frac{1}{r}\frac{\partial}{\partial r}(rj_{ari})+\frac{\partial j_{azi}}{\partial z}\right\}+\dot{q} \qquad (9)$$

where $\dot{q}$ denotes the heat production term of chemical reactions. In this equation $j_{ari}$, $j_{azi}$, $q_r$, and $q_z$ are expressed as follows:

$$j_{ari}=\rho h_i D_i \frac{\partial Y_i}{\partial r} \qquad (10)$$

$$j_{azi}=\rho h_i D_i \frac{\partial Y_i}{\partial z} \qquad (11)$$

$$q_r=\kappa \frac{\partial T}{\partial r} \qquad (12)$$

$$q_z=\kappa \frac{\partial T}{\partial z} \qquad (13)$$

Conservation equations of chemical species are

$$\frac{\partial \rho_i}{\partial t}+\frac{1}{r}\frac{\partial r\rho_i v_r}{\partial r}+\frac{\partial \rho_i v_z}{\partial z}=-\left\{\frac{1}{r}\frac{\partial}{\partial r}(rj_{bri})+\frac{\partial j_{bzi}}{\partial z}\right\}+\dot{\omega} \qquad (14)$$

where $\dot{\omega}$ is the production rate of species by reactions. In this equation, $j_{bri}$ and $j_{bzi}$ are expressed as follows:

$$j_{bri}=\rho D_i \frac{\partial Y_i}{\partial r} \qquad (15)$$

$$j_{bzi}=\rho D_i \frac{\partial Y_i}{\partial z} \qquad (16)$$

Equations are discretized by second-order central differences, and Harten Yee's upwind total variation diminishing (TVD) scheme [21] is employed to capture the shock motion. For simplicity, effects of natural convection and radiation have been ignored. Transport coefficients for the mixture gas like viscosity $\mu$, thermal conductivity $\kappa$, and diffusion coefficient $D_i$ are derived from the approximation formula based on the kinetic theory of gas using Lennard–Jones (12-6) potential [22]. The specific heat of each species is assumed to be a function of the temperature used in CHEMKIN [23]. In the temperature range over 5000 K, the specific heat of each species is extrapolated by the linear function. The mixture used in this study is methane and air, and the equivalence ratio is varied. The chemical reaction scheme for methane/air mixture consists of 34 chemical species and 164 elementary reactions [24]. The time operator for the chemical source term and fluid term is split. Discretization of the reactive source term by chemical reactions has been implicitly conducted by using backward differentiation formula method [25]. To integrate all of the conservation equations, the fourth-order Runge–Kutta method has been employed. The time step in the energy application process is 2.5 ns, and following that it has been varied up to about 12 ns under the limitation of correct calculations.

## III. Results and Discussion

### A. Comparison of OH Concentration Between Numerical and Experimental Measurement for Hydrogen/Air Mixture

In this study, the treatment of the plasma physics may be oversimplified. To verify the performance of the numerical model in this study, we conduct a calculation for a well-characterized configuration of spark ignition process for hydrogen/air mixtures. In the case of methane/air mixtures, quantitative data of radical distributions are rare especially in the early stage of the flame kernel initiation, and therefore the validation of this numerical method is conducted for hydrogen/air mixtures. Although the chemistry of methane is different from that of hydrogen, the detailed models of elementary reactions are used for both of hydrogen and methane mixtures. Main differences are chemical induction time and diffusion characteristics are rather different. Induction time of chemical reactions for hydrogen/air mixtures is much shorter and fuel diffusion is also rather fast. Kinetics of hydrogen chemistry, which consists of 10 species and 27 elementary reactions [26], are taken into account and a model of the thermal diffusion [27,28] is also taken into account for the calculation of the hydrogen mixture. Ono and Oda provide a quantitative distribution of OH density for a hydrogen/air mixture in the spark ignition process [29]. The numerical grids are specialized for the experimental configuration and the number of grids is 150 × 150. The outer boundary in this calculation is nonreflecting boundary. Except for the model of thermal diffusion, numerical grids, the outer boundary, and chemical reactions, the numerical code is completely same as that for methane/air mixtures. In this case, OH density is measured by the laser induced fluorescence (LIF) method and the ignition energy is close to the minimum one. Figure 2 shows distribution fields of OH density for hydrogen (30% in volume)/air mixture with the ignition energy of $1.5E_{\mathrm{min}}$. These series of numerical OH density are equivalent to direct images measured by LIF method in the study by Ono and Oda [29]. When we compare calculated distribution fields of OH density with the experimental ones, numerical results agree well with experimental results in terms of the kernel size and the shape. The qualitative behavior of the hot gas in the initial stage is well expressed by our numerical model. Figure 3 shows time history of OH density for $1.25E_{\mathrm{min}}$. Plots show experimental results [29] and solid line shows numerical one. In [29], the point where OH density is measured is not clear and the variation of OH density in the hot gas is not clear due to the width of the laser sheet (2 mm). Therefore, we use the history of OH density at the center of the hot gas. It can be seen that there is a quantitative difference between experimental and numerical results although the order of OH density is not so different. However, a same tendency can be observed. Firstly, OH density decreases rapidly and then it increases gradually. It reaches to the peak at until 100 $\mu$s and it decreases gradually. The moment when OH density shows minimal is same between numerical and experimental results. Although the treatment of the plasma physics in

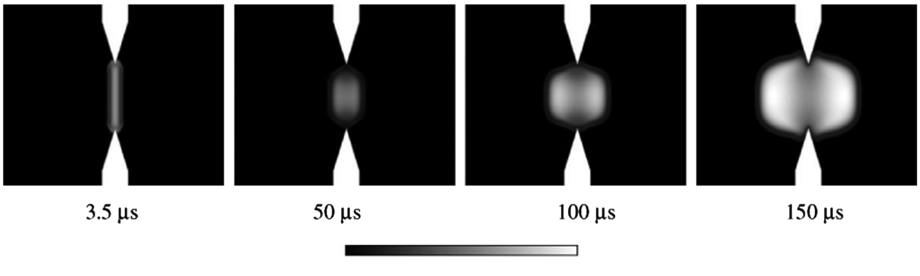

**Fig. 2 Distribution of OH density for $H_2$ (30%)/air mixture with ignition energy of $1.5E_{\mathrm{min}}$.**

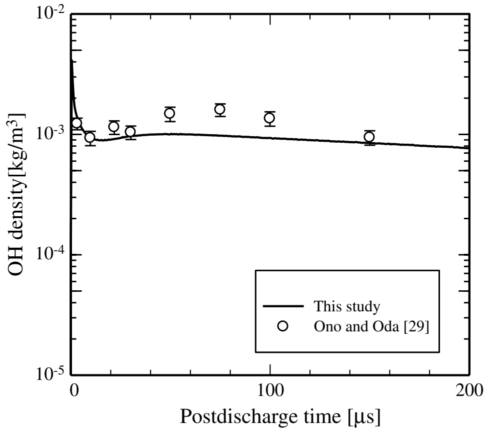

**Fig. 3 History of OH density for $H_2$ (30%)/air mixture with ignition energy of $1.25E_{\min}$. Calculated OH density refers to that at center of electrode gap.**

this study is simple, it is possible to investigate the qualitative behavior of the flame kernel initiation. Therefore, we conduct the numerical analysis for the spark ignition process of methane/air mixtures by using this numerical method.

### B. Calculations of Flame Kernel Initiation and Minimum Ignition Energy for Methane/Air Mixture

The prediction of the qualitative behavior of the flame kernel initiation for hydrogen/air mixtures agrees well with experimental results. Thereby, we conduct the numerical analysis for methane/air mixtures by using the same assumption of the calculation as that for hydrogen/air mixtures. The ignition energy applied in the electrode gap is varied and the process of the flame kernel initiation is investigated. Firstly, the high ignition energy, which is about 100 times higher than the minimum one, is applied in the electrode gap and the intensive behavior of the hot gas expansion is observed. Figure 4 shows the history of the temperature fields and the distribution of velocity vectors for a mixture of 10% volume of methane in air. The ignition energy in this condition is 45.73 mJ, and this figure shows intensive ignition behavior. To compare with each figure, the color bar of the figure is set from 298 to 5000 K and the color of temperature fields at the hot gas region is saturated until 7.23 $\mu$s. The equivalence ratio of the mixture is 1.053 and the adiabatic flame temperature of the methane/air mixture has the peak at this vicinity. The maximum temperature, which is about 9000 K, is observed at 1.00 $\mu$s and it decreases rapidly. In this temperature range, the reaction mechanism is not clear, however, endothermic reactions are thought to be very active and temperature of hot gas rapidly decreases in short time. Initially, the pressure wave of cylindrical geometry with no momentum in the $z$-axis direction is produced. Behind the pressure wave at the initial stage, the strong flowfield is formed. A pair of vortices that rotate in opposite directions forms in the vicinity of the electrode corner. These vortices were observed experimentally, and predicted by Kono et al. [7] and Kravchik and Sher [8]. The hot gas expands rapidly, and the shape is deformed by the flowfields. In this period, the hot gas is strongly affected by the flowfield induced by the blast wave. After the spark discharge is ended, the maximum temperature of the hot gas decreases with time and approaches the flame temperature. In this calculation, numerical domain is bounded by the adiabatic wall, and the pressure wave travels back and forth until the wave decays. Although the hot gas expansion is enhanced toward to the $r$-axis, its development along with the electrode surface is suppressed. This has been predicted by Thiele et al. [10,11]. In this case, the hot gas which expands out of the electrode gap does not quench and the flame propagation starts from this region.

The process of the flame kernel initiation for the application of small ignition energy near the minimal is also tested. Figure 5 shows the evolution of the temperature fields and gas velocity after 1.00 $\mu$s, 2.61 $\mu$s, 31.4 $\mu$s, 500 $\mu$s, 2.76 ms and 3.07 ms for a mixture of 10% methane in air. In this case, ignition energy of 0.4634 mJ is supplied into the electrode gap. The minimum ignition energy for the mixture of 10% methane in air in this calculation is 0.3582 mJ. The determination of the minimum ignition energy is discussed in the later part. The color bar of the figure is from 298 to 3000 K and the color of temperature fields at the hot gas region is saturated until 2.61 $\mu$s. In this case, induction time of the flame kernel initiation is

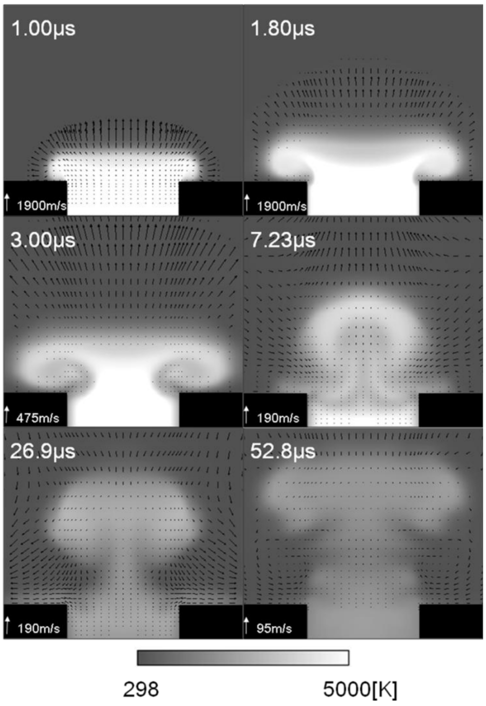

**Fig. 4 Temperature distribution fields for methane/air mixture at 0.1013 MPa after 1.00, 4.65, 25.2, 47.0, 101, and 196 $\mu$s. Equivalence ratio of mixture = 1.053, and ignition energy= 45.73 mJ.**

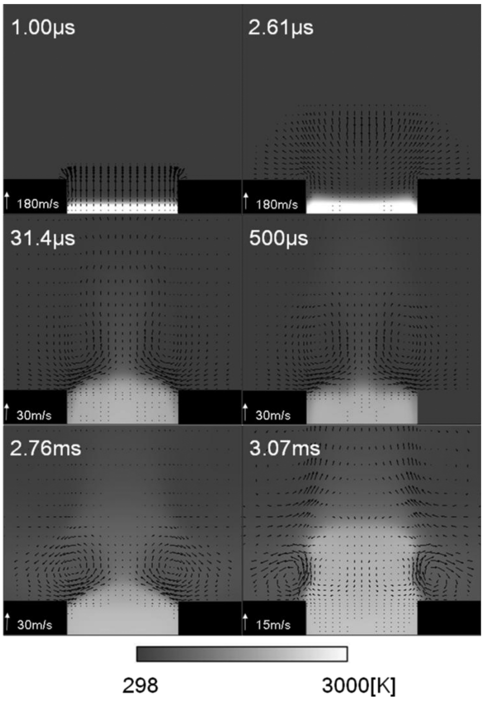

**Fig. 5 Temperature distribution fields for methane/air mixture at 0.1013 MPa after 1.00, 2.61, 31.4, and 500 $\mu$s, and 2.76 and 3.07 ms. Equivalence ratio of mixture = 1.053, and ignition energy= 0.4634 mJ.**

long due to small ignition energy near the minimal. The maximum temperature of the hot gas decreases rapidly after the ignition energy is cut off and reaches a stable value around 2000 K. The hot gas which expands out of the electrode gap quenches rapidly and the hot gas is sustained at the electrode gap. In the early stage, the hot gas expansion is strained by the stretch effects. The chemical reaction in the hot gas region slowly progresses. As a consequence, a reactive flame kernel, which can propagate into the mixture, is formed in the electrode gap. In this figure, the hot gas region starts to expand at 2.76 ms and the flame kernel initiation is achieved. The hot gas region produced by low ignition energy is strongly affected by perturbations such as the diffusion of radicals, flowfields which are directed toward the electrode gap and heat loss to the electrode surface. The area of the hot gas region at 500 $\mu$s is minimal. It takes a lot of time for the flame kernel to be formed in the case of the small ignition energy. In the case of the minimum ignition energy, the same tendency can be observed although the induction time of the flame kernel initiation is longer. This calculation is conducted in a small numerical domain where the shock wave traverses frequently. The effects of the flowfields induced by the blast wave on the flame kernel initiation and chemical reactions can be observed.

Success or failure of the ignition is determined by a history of the total mass of OH which exists in the numerical domain. Figure 6 shows time histories of the total mass of OH for 10% volume of methane in air. The OH mass is integrated throughout the numerical domain. The history of OH mass also shows the condition of the hot gas region in the process of flame kernel development. For the ignition energy of 0.3578 mJ, it can be seen that the total mass of OH increases initially due to the expansion of the hot gas region induced by the blast wave, and gradually it declines after 10 $\mu$s. After 10 $\mu$s; OH production is suppressed by the mixing effect of low and high-temperature gas by the flow and diffusion of radicals. In this case, the hot gas region exists only in the electrode gap and it does not grow out of the gap. A sudden decrease in OH denotes that the hot gas region is quenching and ignition fails in this case. The temperature of the hot gas gradually decreases and is not sustained. On the other hand, for the ignition energy of 0.3582 mJ, the total mass of OH increases and decreases repeatedly, and finally steadily increases. In this case, the growth of the hot gas region is similar with that shown in Fig. 5 although the initial volume of the hot gas is small. When the total mass of OH shows steadily increasing trend, the active flame kernel is formed. This tendency is dominated by the interaction between chemical reactions in the hot gas region and the flowfield. The total mass of OH increases constantly after some time and ignition is successful in this case. For large ignition energy, the total mass of OH fluctuates initially due to the strong shock wave, and in the result it increases. When the flame kernel starts to expand spontaneously, the gradient of the total mass of OH rapidly increases, as can be seen in Fig. 6. Time when total mass of OH finally shows an increase trend is the induction time of the flame kernel initiation. It can be seen that the lower ignition energy requires the longer induction time.

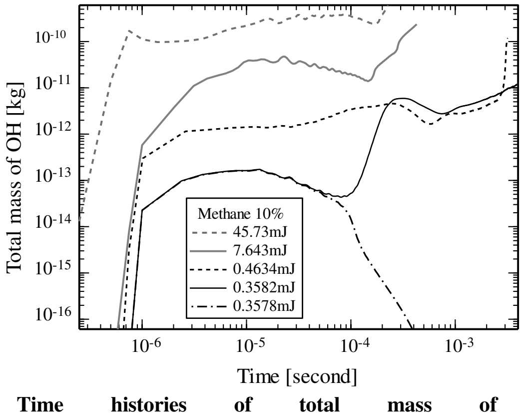

**Fig. 6 Time histories of total mass of OH. Equivalence ratio of mixture = 1.053. Total mass is defined as the amount of OH that exists in the computing region.**

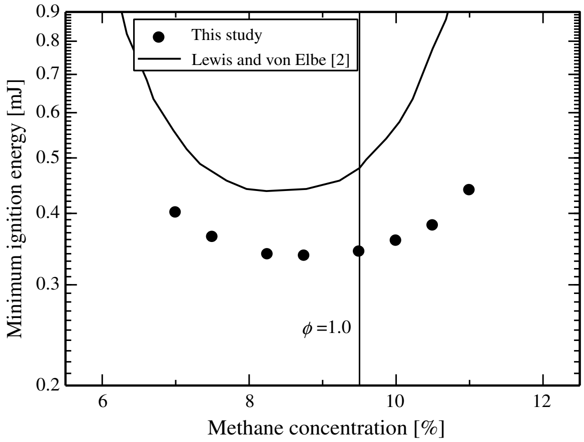

**Fig. 7 Minimum ignition energy for methane/air mixtures at 0.1013 MPa.**

Figure 7 shows the minimum ignition energies for methane/air mixtures at 0.1013 MPa. The solid line in the figure shows the ignition energy measured by Lewis and von Elbe [2]. Although the calculated minimum ignition energy is underestimated in comparison with the experimental one, plots of calculated minimum ignition energy is close to that measured by Lewis and von Elbe qualitatively [2]. The difference is approximately 0.15 mJ for 9.5% of methane in air. In this calculation, there is no convection induced by the gravity and the hot gas exists at the electrode gap. In the case where minimum ignition energy is applied, it takes a lot of time for the flame kernel initiation. The hot gas is not disturbed by the outer flowfield for a long period. In addition, radiation from plasma and chemical species such as $CO_2$, $H_2O$ and $CH_4$ are neglected. Therefore, minimum ignition energy is thought to be lower in this calculation. The solid vertical line in Fig. 7 denotes the line of stoichiometric conditions for the methane/air mixture. The minimum value of minimum ignition energy for methane/air mixtures can be seen in the lean mixture region.

### C. Effects of Diffusion Process on Flame Kernel Initiation for Methane/Air Mixture

To investigate the effect of diffusion of reactants and products on the ignition process, distribution fields of the local equivalence ratio are calculated. The local equivalence ratio $\Phi_l$ is defined as $\Phi_l = (m_F/m_O)/(m_F/m_{Ost})$, where $m_F$, $m_O$ and $m_{Ost}$ denote local mass of carbon (C) and hydrogen (H) atoms, local mass of oxygen (O) atoms and stoichiometric mass of O atoms for C and H atoms, respectively. Chemical reactions in the hot gas are transient and a lot of intermediates are included. All elements even in molecules are taken into account. The local equivalence ratio in each cell does not change without diffusion even when chemical reactions proceed. Thereby, this parameter indicates the excess or short amount of fuel components in cells. Calculating masses of O, C, and H atoms, we can observe the condition of the local mixture and the effect of diffusion in both of the unburnt and the burnt gas regions. When the local equivalence ratio in a cell is higher than the initial equivalence ratio of the mixture, fuel components (radicals and $CH_4$) diffuse into the cell or oxidizer diffused out of the cell. Accumulation behaviors of fuel and oxygen components are shown by this parameter.

Figure 8 shows the distribution fields for the local equivalence ratio after 1.00, 1.80, 3.00, 7.23, 26.9 and 52.8 $\mu$s for the mixture of 10% methane in air with ignition energy of 45.73 mJ. In this case, where large ignition energy is applied to the electrode gap, the diffusion fields for high temperature can be seen. The temperature fields in these figures are shown in Fig. 4. The equivalence ratio of this mixture is 1.053. A region of low $\Phi_l$ along the surface of the active reaction zone is noticeable. This region corresponds to the high heat release area. Therefore, a lot of radicals such as CH and H diffuse rapidly from the reaction zone, whereas products such as carbon dioxide ($CO_2$) and carbon monoxide (CO) diffuse slowly.

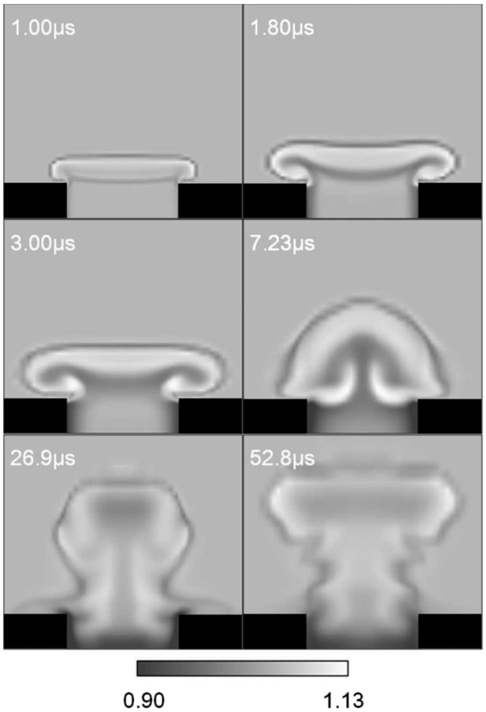

**Fig. 8 Distribution fields of local equivalence ratio for methane/air mixture at 0.1013 MPa after 1.00, 1.80, 3.00, 7.23, 26.9, and 52.8 $\mu$s. Equivalence ratio of mixture = 1.053, and ignition energy= 45.73 mJ.**

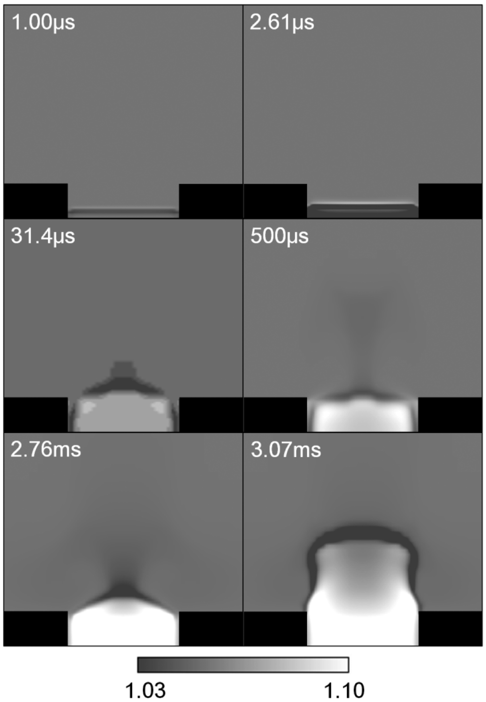

**Fig. 9 Distribution fields of local equivalence ratio for methane/air mixture at 0.1013 MPa after 1.00, 2.61, 31.4, and 500 $\mu$s, and 2.76 and 3.07 ms. Equivalence ratio of mixture = 1.053, and ignition energy= 0.4634 mJ.**

Inside the active reaction zone, a high $\Phi_l$ region can be observed due to diffusion of radicals from the reaction zone. These layers with high and low local equivalence ratio are deformed by the strong flow during short period. On the other hand, $\Phi_l$ at the electrode gap decreases with time due to the diffusion of radicals from the electrode gap. The temperature fields at the electrode gap remain high in this case, and the diffusion of radicals, which are not fully oxidized, is still active. In the case of the high ignition energy, diffusion of radicals is rather active and residential time of radicals is small. Therefore, regions of high and low local equivalence ratio coexist.

Figure 9 shows the distribution fields of the local equivalence ratio after 1.00, 2.61, 31.4, and 500 $\mu$s, and 2.76 and 3.07 ms for a mixture of 10% methane in air with ignition energy of 0.4634 mJ. To highlight the region with the low local equivalence ratio, the color bar of this figure is set from 1.03 to 1.10. The temperature fields in this case are shown in Fig. 5. In this case, ignition energy is low, and the distribution fields of $\Phi_l$ for low ignition energy are observed. $\Phi_l$ at the electrode gap and the boundary between high- and low-temperature regions is minimal. However, $\Phi_l$ at the entire region of the electrode gap increases up to approximately 1.12 with time. When the active flame kernel is developed in Fig. 9, a low $\Phi_l$ region at the active reaction zone is also observed, however, a high $\Phi_l$ region at the electrode gap is still present. Outside the hot gas region, the gas with low $\Phi_l$ region is widespread and convected outward by the flow. In the case of small ignition energy, the induction time when the active flame front is developed is rather long. It is over 500 $\mu$s at which total mass of OH starts to increase with the ignition energy of 0.4634 mJ. Since the flowfield induced by the blast wave is weak, the role of diffusion process in the flame kernel development becomes important due to the longer induction time. Besides the large induction time, rates of chemical reactions are slow due to low temperature of the hot gas region. Concentration of radicals with ignition energy of 0.4634 mJ is much smaller than that with higher ignition energy. Therefore, diffusion rate of radicals from the hot gas region to ambient gas is small. In addition, although methane is cracked and its concentration is low at the high-temperature region of the electrode gap, it is also supplied by the preferential diffusion from the outer mixture and is subsequently accumulated. Diffusion rate of methane to the hot gas region is faster than that of oxygen. Local equivalence ratio becomes higher in the electrode gap than in the ambient gas due to the accumulation of methane. The ambient gas near the electrode gap is transported by the flow. Therefore, the region with low $\Phi_l$ is widely observed outside the hot gas region.

For further understanding of the effect of diffusion of molecules in the flame kernel initiation, scatter plots of the local equivalence ratio and temperatures are shown in Fig. 10. Plots with high ignition energy of 45.73 mJ at 52.8 $\mu$s, intermediate ignition energy of 7.643 mJ at 59.9 $\mu$s and low ignition energy of 0.4634 mJ at 500 $\mu$s are scattered in the figure. The number of plots in the figure is equal to the number of grids. In the case of the intermediate energy application, the flame kernel initiation starts in the hot gas region which spurts out of the electrode gap. The tendency of the flame kernel initiation is same as that in the case of the high-energy application. In the case of the high-energy application, plots scatter widely due to the fast expansion of the hot gas region and strong flow. In addition, the temperature of the hot gas region is high and the production of radicals is rather active. Therefore, diffusion of radicals is rather active and regions with high and low local equivalence ratios coexist, and the range of the local equivalence ratio is wide. On the other hand, in the case of the low energy application, the local

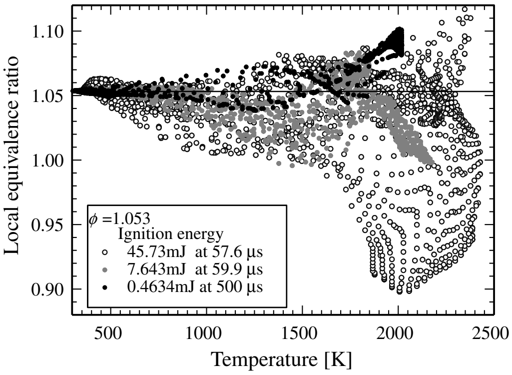

**Fig. 10 Scatter plots of temperature and local equivalence ratio. Equivalence ratio of mixture = 1.053.**

equivalence ratio in the high-temperature region is over 1.053. The production of radicals is not active and the diffusion of methane into the hot gas region is recognized. In addition, the low-temperature region around the hot gas has low equivalence ratio and the plots with the local equivalence ratio below 1.053 are located in low-temperature region. Compared with plots in the case of high ignition energy, the distribution range of the local equivalence ratio is narrow. Local variation of the equivalence ratio is mitigated during long induction time and the accumulation of molecules in the hot gas region is observed. In the case of hydrogen/air mixture, the same kind of fuel accumulation is also clearly observed for shorter period of time. The rate of diffusion for hydrogen molecules and atoms are rather fast compared with methane and it is also affected by thermal diffusion. Therefore, the effect of the accumulation on flame kernel initiation process is outstanding for lighter molecules and small ignition energy.

## IV. Conclusions

A numerical study to simulate the spark ignition for methane/air mixtures has been conducted. An element reaction model of methane combustion was used in this study. To capture the behavior of the blast wave, TVD scheme was used in the evaluation of the numerical flux. A theoretical model of transport and thermodynamics parameters has also been integrated into the numerical code. Plasma physics in our model might be oversimplified; the predicted behavior of OH density with small ignition energy shows a good agreement with the sophisticated experimental measurements [29].

The development of the flame kernel for a methane/air mixture is strongly influenced by the blast wave and the induced flowfields. The shape and propagation of the flame kernel is dominated by the flowfields in the case of large ignition energy, whereas a certain delay of the flame kernel initiation can be observed in the case of low ignition energy. When the active flame kernel is developed, the total mass of OH, which is integrated through the numerical domain, increases rapidly. When spark energy located slightly below the minimum ignition energy is applied to the electrode gap, the total mass of OH decreases rapidly after a certain delay.

The calculated profile of the minimum ignition energy as a function of the equivalence ratio for methane/air mixtures is similar to experimental ones measured by Lewis and von Elbe [2]. As a result, the minimum value of the calculated minimum ignition energy for the methane concentration is also evaluated in the lean concentration. Although the local equivalence ratio at the electrode gap decreases far more than that of the ambient mixture for high ignition energy, the local equivalence ratio inside the flame front is larger than the ambient one. Regions with high and low equivalence ratio locally coexist due to the strong flow and short induction time. For low ignition energy, the local equivalence ratio at the entire region of the electrode gap is larger than the ambient one. Preferential diffusion of methane into the reaction zone at the electrode gap is clearly observed in the numerical results and the effect of diffusion on ignition process for methane/air mixtures with low ignition energy can be realized.

## References

[1] Ono, R., Mifuku, M., Fujiwara, S., Horiguchi, S., and Oda, T., "Minimum Ignition Energy of Hydrogen–Air Mixture: Effects of Humidity and Spark Duration," *Journal of Electrostatics*, Vol. 65, No. 2, 2007, pp. 87–93. doi:10.1016/j.elstat.2006.07.004

[2] Lewis, B., and von Elbe, G., "*Combustion Flames and Explosions of Gases*, 3rd ed., Academic Press, Orlando, FL, 1987.

[3] Sloane, T. M., "Numerical Simulation ot Electric Spark Ignition in Atmospheric Pressure Methane/air Mixtures," *Combustion Science and Technology*, Vol. 73, No. 1, 1990, pp. 367–381. doi:10.1080/00102209008951657

[4] Kono, M., Hatori, K., and Iinuma, K., "Investigation of Ignition Ability of Composite Spark in Flowing Mixture," *Proceedings of the Combustion Institute*, Vol. 20, 1984, pp. 133–140.

[5] Ishii, K., Aoki, O., Ujiie, Y., and Kono, M., "Investigation of Ignition by Composite Sparks under High Turbulence Intensity Conditions," *Combustion and Flame*, Vol. 91, No. 2, 1992, pp. 153–163. doi:10.1016/0010-2180(92)90097-9

[6] Yuasa, T., Shinichi, K., Tsue, M., Kono, M., Nomura, H., and Ujiie, Y., "Effects of Energy Deposition Schedule on Minimum Ignition Energy in Spark Ignition of Methane/Air Mixtures," *Proceedings of the Combustion Institute*, Vol. 29, 2002, pp. 743–750. doi:10.1016/S1540-7489(02)80095-5

[7] Kono, M., Niu, K., Tsukamoto, T., and Ujiie, Y., "Mechanism of Flame Kernel Formation Produced by Short Duration Spark," *Proceedings of the Combustion Institute*, Vol. 23, 1988, pp. 1643–1649.

[8] Kravchik, T., and Sher, E., "Numerical Modeling of Spark Ignition and Flame Initiation in a Quiescent Methane/Air Mixture," *Combustion and Flame*, Vol. 99, Nos. 3–4, 1994, pp. 635–643. doi:10.1016/0010-2180(94)90057-4

[9] Sher, E., and Refael, S., "Numerical Analysis of the Early Phase Development of Spark-Ignited Flames in CH4-Air Mixture," *Proceedings of the Combustion Institute*, Vol. 19, 1982, pp. 251–257.

[10] Thiele, M., Warnatz, J., Dreizler, A., Lindenmaier, S., Shiebl, R., Maas, U., Grant, A., and Ewart, P., "Spark Ignited Hydrogen/Air Mixtures: Two Dimensional Detailed Modeling and Laser Based Diagnostics," *Combustion and Flame*, Vol. 128, Nos. 1–2, 2002, pp. 74–87. doi:10.1016/S0010-2180(01)00333-9

[11] Thiele, M., Selle, S., Riedel, U., Warnatz, J., and Maas, U., "Numerical Simulation of Spark Ignition Including Ionization," *Proceedings of the Combustion Institute*, Vol. 28, 2000, pp. 1177–1185. doi:10.1016/S0082-0784(00)80328-8

[12] Kono, M., Hatori, K., and Iinuma, K., "Investigation of Ignition Ability of Composite Sparks in Flowing Mixtures," *Proceedings of the Combustion Institute*, Vol. 20, 1984, pp. 133–140.

[13] He, L., "Critical Conditions for Spherical Flame Initiation in Mixtures with High Lewis Numbers," *Combustion Theory and Modeling*, Vol. 4, No. 2, 2000, pp. 159–172. doi:10.1088/1364-7830/4/2/305

[14] Chen, Z., and Ju, Y., "Theoretical Analysis of the Evolution from Ignition Kernel to Flame Ball and Planar Flame," *Combustion Theory and Modeling*, Vol. 11, No. 3, 2007, pp. 427–453. doi:10.1080/13647830600999850

[15] Kelley, A. P., Jomaas, G. J., and Law, C. K., "Critical Radius for Sustained Propagation of Spark-Ignited Spherical Flames," *Combustion and Flame*, Vol. 156, No. 5, 2009, pp. 1006–1013. doi:10.1016/j.combustflame.2008.12.005

[16] Bradley, D., and Lung, F. K.-K., "Spark Ignition and the Early Stages of Turbulent Flame Propagation," *Combustion and Flame*, Vol. 69, No. 1, 1987, pp. 71–93. doi:10.1016/0010-2180(87)90022-8

[17] Huang, C. C., Shy, S. S., Liu, C. C., and Yan, Y. Y., "A Transition on Minimum Ignition Energy for Lean Turbulent Methane Combustion in Flamelet and Distributed Regimes," *Proceedings of the Combustion Institute*, Vol. 31, 2007, pp. 1401–1409. doi:10.1016/j.proci.2006.08.024

[18] Frendi, A., and Sibulkin, M., "Dependence of Minimum Ignition Energy on Ignition Parameters," *Combustion Science and Technology*, Vol. 73, No. 1, 1990, pp. 395–413. doi:10.1080/00102209008951659

[19] Wang, C.-S., and Sibulkin, M., "Comparison of Minimum ignition Energy for Four Alkanes: Effects of Ignition Kernel Size and Equivalence Ratio," *Combustion Science and Technology*, Vol. 91, No. 1, 1993, pp. 163–178. doi:10.1080/00102209308907638

[20] Mary, R., *Spark Ignition: its Physics and Effects on the Internal Combustion Engine, Fuel Economy in Road Vehicles Powered by Spark Ignition Engines*, Pleum Press, New York, 1984.

[21] Yee, H., "Upwind and Symmetric Shock Capturing Schemes," NASA TM 89464, 1987.

[22] Reid, R. C., Plausnitz, J. M., and Poling, B. E., *The Properties of Gases and Liquids*, McGraw–Hill, New York, 1988.

[23] Kee, R. J., Rupley, F. M., and Miller, J. A., "CHEMKIN-II: A Fortran Chemical Kinetics Package for the Analysis of Gas-Phase Chemical Kinetics," Sandia National Laboratories Rept. No. SAND 89-8009, 1989.

[24] Warnatz, J., Maas, U., and Dibble, R. W., *Combustion; Physical and Chemical Fundamentals, Modeling and Simulation, Experiments, Pollutant Formation*, 3rd ed., Springer, Berlin, 2000, p. 69.

[25] Oran, E. S., and Boris, J. P., *Numerical Simulation of Reactive Flow*, 2nd ed., Cambridge Univ. Press, Cambridge, U. K., 2001, p. 133.

[26] Marinov, N., Westbrook, C. K., and Pitz, W. J., *Transport Phenomena in Combustion*, edited by S. H. Chan, Vol. 1, Taylor and Francis, Washington, D.C., 1996.

[27] Kee, R. J., Lewis, G. D., and Warnatz, J., "A Fortran Computer Code Package for the Evaluation of Gas-Phase Multicomponent Transport Properties," SAND 86-8246B, 1986.

[28] Neufeld, P. D., and Janzen, A. R., "Empirical Equations to Calculate 16 of the Transport Collision Integrals $\Omega^{(l,s)*}$ for the Lennard–Jones (12-6) Potential," *Journal of Chemical Physics*, Vol. 57, No. 3, 1972, pp. 1100–1102.
doi:10.1063/1.1678363

[29] Ono, R., and Oda, T., "Measurement of OH Density and Gas Temperature in Incipient Spark-Ignited Hydrogen–Air Flame," *Combustion and Flame*, Vol. 152, Nos. 1–2, 2008, pp. 69–79.
doi:10.1016/j.combustflame.2007.07.022

A. Gupta
*Associate Editor*